HAPKE SPECTRAL MODELING OF THE SPACE WEATHERED SURFACE OF MERCURY CONSTRAINED BY COMPOSITIONAL INFORMATION FROM MESSENGER. K. R. Stockstill-Cahill[1], N. R. Izenberg[2], D. Trang[3], J. T. S. Cahill[2], and D. Domingue[1], [1]Planetary Science Institute (1700 East Fort Lowell, Suite 106, Tucson, AZ 85719), [2]JHU/Applied Physics Laboratory, [3]UH-Manoa, HIGP.

Introduction: Using orbital data from the Mercury Surface, Space ENvironment, GEochemestry, and Ranging (MESSENGER) mission, [1,2] identified distinct geochemical regions using the X-ray Spectrometer (XRS) and Gamma-Ray and Neutron Spectrometer (GRNS) data. Normative analyses of the elemental composition data for nine distinct geochemical regions were used to constrain the mineralogy present at Mercury's surface [2] yielding mineralogies dominated by silicates (plagioclase, pyroxene, olivine, quartz). Starting with these mineralogies, we used the Hapke radiative transfer model [3-5] to predict bidirectional reflectance spectra in a forward modeling approach [6,7].

In Hapke's model, the reflectance spectrum of a regolith is computed linearly from the single-scattering albedos (SSA) of mineral end-members [4,5]. The SSA is the probability that a photon incident on a regolith particle will be scattered rather than absorbed. It is independent of illumination or viewing geometry and a function of a grain's scattering behavior and absorption coefficient. The absorption coefficient is governed by the material's complex index of refraction, which is a function of the optical constants. Optical constants are wavelength-dependent quantities unique to each particle type in a regolith and represent the inherent physical and chemical properties of each material [8].

In order to accurately interpret reflectance spectra for airless bodies, the effects of opaque phases (e.g., Fe, Ni, sulfides) must be properly considered. Opaque metals are present as native igneous minerals in meteorites and on planetary surfaces in the form of grains that are significantly larger than the wavelength of the incident light. However, nanophase metal grains are a key by-product of space weathering [5,9-11] and introduce confounding effects on ultraviolet (UV), visible (VIS), and near-infrared (NIR) spectra as seen in laboratory measurements and spacecraft observations.

To address this issue, our model also included optical constants for opaque metal and mineral phases. Metals are present in planetary regolith in three spectrally-significant grain size categories: macroscopic, microphase, and nanophase [5,12-17]. Macroscopic metal particles are large relative to the wavelength of light and grains of this size are often found as native igneous species in meteorites and lunar samples [18]. Microphase particles (mp-) have diameters from ~50 nm to ~3000 nm, produce an overall decrease in reflectance with few effects on the continuum slope of a spectrum [11,16,17]. Finer-grained opaques (<50 nm in diameter) is referred to as "nanophase metal" (np-) and decreases the overall reflectance and introduces a strong positive spectral slope across the visible to NIR (i.e., spectral "reddening") [10, 11].

Global maps of space weathering products ($npFe^0$, npC, $mpFe^0$, and mpC) for Mercury were produced using radiative transfer models of MESSENGER's VIRS data [19]. This study used an average "starting" albedo of 80% and added nano- and microphase particles using [5,17] and demonstrated that all four phases are needed to reproduce the low albedo of Mercury.

This study uses these same space weathering products, but models a "starting spectrum" generated from the mineralogy of [2]. This technique provides improved contraints on space weathering components because the average albedo derived for the mineralogies of [2] is 53.2 ± 2.0% (*Table 1*), much lower than the 80% used in [19]. Also, the starting spectrum will have the pre-existing slope and shape upon which the darkening and reddening of space weathering components will be overprinted (*Figure 1*).

Table 1: Albedo (300-850 nm) calculated from minerologies derived for the surface types by [2]

Surface types [1,2]	Average albedo	Min albedo	Max albedo
HMR	52.4	12.2	56.9
HMR-CaS	51.3	12.1	55.5
CB	51.5	10.7	55.6
RB	53.1	12.0	57.8
PD	53.9	11.7	58.9
HAI	57.0	10.6	63.7
NP-LMg	53.4	10.2	58.7
NP-HMg	55.3	11.4	61.0
IT	50.8	11.2	54.7
Avg all ST	53.2	11.4	58.1
Stdev	2.0	0.7	2.9

Methods: The model used was adapted from the work of [20], which uses optical constants for metals (Fe, Ni) to introduce the darkening and/or reddening effects of microscopic and nanophase metal on a reflectance spectrum. Required inputs are the abundance and composition of phases (including plagioclase, ilmenite, olivine, orthopyroxene, clinopyroxene, glass, agglutinates, macrometal, nanophase metal, microphase metal) as well as the grain sizes of the (macrophase) host particles and the microphase metal.

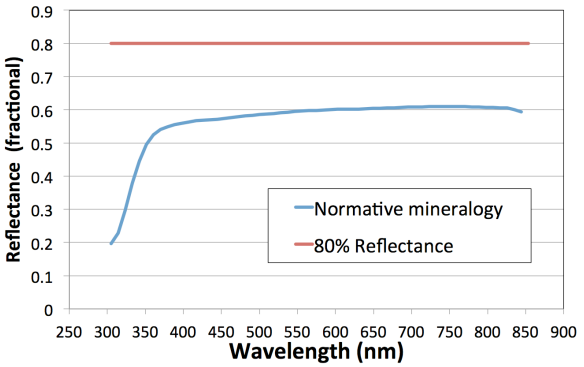

Figure 1: Reflectance spectrum derived from Rachmaninoff Basin mineralogy [2] (blue) compared to 80% reflectance (red).

We adapted the algorithm for applications to other airless planetary bodies, including Mercury. For this study, we sought to extend the opaque phases available for spectral mixing and space weathering, which were previously centered on the Fe-rich nature of the Moon. Specifically, we allow for sulfides as a macrophase opaque. In addition, we have added amorphous carbon as a possible space weathering component and allowed for two nanophase and two microphase components to be included after the results of [3].

The SNR of the VIRS NIR detector was 3-5 times lower than that of the VIS detector [21] due to the NIR detector being more sensitive to elevated temperature and background noise. Therefore, we modeled only the visible region (300-850 nm) of each VIRS spectrum. Furthermore, we adopted the practice of avoiding data covering polar latitudes (>70°), which were observed at very high incidence angles that resulted in shadowing effects in the observations [21]. Finally, we applied a 4-band boxcar filter to spectral data of individual units to reduce band-to-band variations present in the data set while still maintaining the overall spectral shape and absorptions present. Results of these models for MASCS spectra will be presented.

Rachmaninoff Basin: The Rachmaninoff Basin region is prominent for its high Mg/Si outside the high Mg region [1]. The peak ring contains relatively young volcanic smooth plains and differs markedly in albedo from the surrounding annular ring plains [22], which match the spectral properties of the LRM [23]. Weider *et al.* [1] suggested that this impact excavated an Mg-rich magmatic body with sulfides representing the darkening agent. Normative analysis for Rachmaninoff Basin (Table 2) spans the boundary between komatiites and boninites [2].

Results: Intial results for modeling the MASCS spectrum for Rachmaninoff Basin are shown in Figure 2. This model included the normative mineralogy [2] and 10% agglutinates and no macrometal. The best fit

Table 2: Normative mineralogy derived for Rachmaninoff Basin from [2]			
Plagioclase	42%	**Hypersthene**	11%
Olivine	24%	**Sulfides**	5%
Diopside	16%	**Opx**[1]	1%

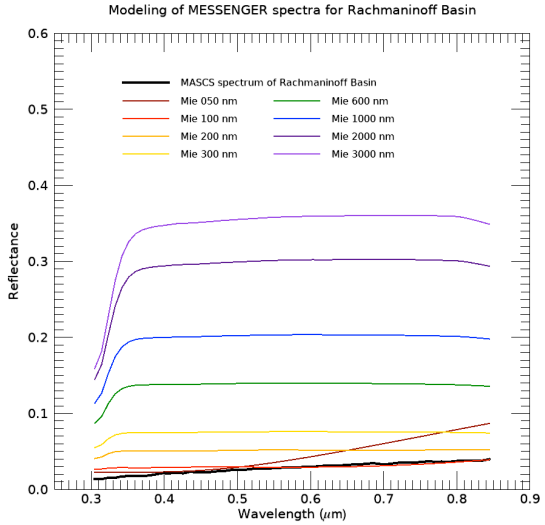

Figure 2: Initial spectral modeling results for Rachmaninoff Basin showing the effects of a range of microphase particle sizes (50-3000 nm).

additional iterations will be done in order to improve the fit. Certain adjustments can be done, including increasing the amount of agglutinates and macrophase metal. The abundance of these two phases can be further contrained by the environment at Mercury and the compositional contraints provided by MESSENGER.

References: [1] Weider et al. (2015) *EPSL*, 416, 109-120. [2] Vander Kaaden et al. (2016) *Icarus, 285*, 155-168. [3] Hapke (1981) *JGR, 86*, 3039–3054. [4] Hapke (1993) *Theory of Reflectance and Emittance Spectroscopy*, Cambridge Univ. Press, U.K. [5] Hapke (2001) *JGR, 106*, 10,039–10,073. [6] Lucey (1998) *JGR*, *103*, 3679–3699. [7] Wilcox et al. (2006) *JGR*, *111*. [8] Palik (1991) *Handbook of Optical Constants v.2*, Academic Press, Boston. [9] Keller & McKay (1997) *GCA, 61*, 2331–2341. [10] Pieters et al. (2000) *MaPS, 35*, 1101–1107. [11] Noble et al. (2007) *Icarus*, 192, 629–642. [12] Britt & Pieters (1994) *GCA, 58*, 3905–3919. [13] Pieters et al. (2000) *MaPS*, *35*, 1101–1107. [14] Noble & Pieters (2003) *JGR, 111*. [15] Nobel et al. (2006) *JGR*, *111*. [16] Lucey & Noble (2008) *Icarus*, *197(1)*, 348–353. [17] Lucey & Riner (2011) *Icarus*, *212*, 451–462. [18] Lawrence & Lucey (2007) *JGR, 112*. [19] Trang et al. (2017) *Icarus, 293,* 206-17. [20] Cahill et al. (2015) *JGR, 115*. [21] Izenberg et al. (2014) *Icarus*, 228, 364-374. [22] Prockter et al. (2010) *Science*, 329, 668-671. [23] Denevi et al. (2009) *JGR*, 118, 891-907.